



Enhancement of spin-orbit torque in WS₂/Co/Pt trilayers via spin-orbit proximity effectYuzhi Li , Yakai Song, Jianrong Zhang, Qiu Yang, Li Xi , Yalu Zuo,
Junli Zhang, Mingsu Si , Desheng Xue,^{*} and Dezheng Yang [†]*Key Laboratory for Magnetism and Magnetic Materials of Ministry of Education, Lanzhou University, Lanzhou 730000, China*

(Received 27 October 2022; revised 15 February 2023; accepted 16 February 2023; published 7 March 2023)

Enhancement of spin-orbit torque (SOT) efficiency in ferromagnet/heavy-metal bilayer is promising for the realization of low-power spintronic devices. Here we show that inserting a single-layer WS₂ between the substrate and Co/Pt layers, can reduce Co coercivity by $\sim 28\%$ and increase dampinglike SOT efficiency by $\sim 30\%$, up to $35.07 \text{ Oe}/(10^7 \text{ A/cm}^2)$. When inserting WS₂ with different layers, we further demonstrate that these phenomena only exist for odd WS₂ layers, i.e., monolayer and trilayer, while they disappear for even WS₂ layers, i.e., bilayer. Theoretical analysis based on the first-principles calculations suggests that the results originate from the thickness-controlled charge transfer between WS₂ and Co, which is consistent with the spin-orbit proximity effect.

DOI: [10.1103/PhysRevB.107.L100403](https://doi.org/10.1103/PhysRevB.107.L100403)

Increasing spin-orbit torque (SOT) efficiencies for lowering current density is of great importance for advancing technological applications and for enabling new research on spintronics phenomena [1,2]. Research in ferromagnet (FM)/heavy-metal (HM) bilayer have shown that engineering interface to manipulate spin current is a powerful way to increase SOT performance, such as adjusting surface roughness [3], varying the thickness of HMs [4], pairing two HMs with opposing spin Hall angles [5], and inserting the interface layers [6,7]. Moreover, engineering interfaces can also generate spin current by different mechanisms. For example, due to the spin-momentum lock effect at the topological surface states, the topological insulators may have a greater charge-to-spin conversion ratio than HM [8,9]. Even for 3d transitional metals with weak spin-orbit coupling (SOC) such as Ti, V, and so on, they have exhibited a significant SOT by the orbit-Hall effect [10,11]. Moreover, interface-induced spin current has been observed in FM/nonmagnetic light metal bilayer by reducing system symmetry [12,13].

Due to the large SOC, two-dimensional (2D) materials of transition-metal dichalcogenides (TMDs) are also very promising candidates for the SOT device [14–16]. As a pioneering work, Shao *et al.* have reported a SOT generated by the Rashba interaction in the TMD/FM bilayer device [14]. For MoS₂/CoFeB and WSe₂/CoFeB, the field-like SOT efficiencies are 0.78 and $1.14 \text{ Oe}/(10^7 \text{ A/cm}^2)$, respectively, even comparable to $0.90 \text{ Oe}/(10^7 \text{ A/cm}^2)$ for Ta/CoFeB. Owing to the breaking symmetry of the WTe₂ lattice structure, the out-of-plane polarized spin current is also demonstrated in WTe₂/Py bilayers, when applying current along the low-symmetry axis of WTe₂ [17–19]. The control of spin polarized direction has also been achieved by the symmetry designs, i.e., the magnetic spin Hall effect with breaking

time-reversal symmetry [20]. Besides being the spin current source, the TMDs can also be considered as a spin sink for the substrate/TMD/HM/FM structure. Since WSe₂ strongly decreases the opposite spin current flow back, the SOT efficiency of substrate/WSe₂/Ta/CoFeB is 26.5 times larger than that of Ta/CoFeB, up to $57.50 \text{ Oe}/(10^7 \text{ A/cm}^2)$ [21]. Similar results have also been reported in substrate/WSe₂/Pt/Co heterostructures [22], in which the SOT efficiency enhances with increasing the thickness of WSe₂.

Recently, the spin-orbit proximity effect (SOPE) is theoretically predicted in TMDs/ultrathin FM bilayer [23]. Owing to the hybridization of the wave function of FM and TMDs, a nonequilibrium spin density can occur in such a heterostructure. It not only induces a local magnetic moment in TMDs, similar to the magnetic proximity effect [24,25], but also leads to an additional SOT [23,26]. At the interface of TMDs/FM, the proximity spin-orbit coupling can directly induce in-plane spin textures of FM, and change the electronic and spin structure of FM within some distance away from the interface. Unlike the fixed polarization of spin current in the FM/HM bilayer, the polarization of spin current due to SOPE can be controlled, which depends on the magnetization [26]. Such arbitrary spin polarization directions can induce efficient and deterministic switching [27,28]. So far, the corresponding experiment is still lacking. Therefore, it is crucial to experimentally explore the SOPE inducing SOT in TMD/FM/HM heterostructure.

In this work, we experimentally investigate the SOPE in the WS₂/Co/Pt trilayers SOT devices with in-plane anisotropy by varying the layer counts of WS₂ (0–3 L). We find that the dampinglike SOT efficiency has been obviously enhanced, accompanying with the reduction of coercivity. The enhanced SOT and reduced coercivity both have the identical dependence on WS₂ layer counts, where the variation of the odd layer counts of WS₂ (1 and 3 L) is much larger than the even layer counts (2 L). The charge density difference based on the first-principles calculations directly shows that the charge

^{*}xueds@lzu.edu.cn[†]yangdzh@lzu.edu.cn

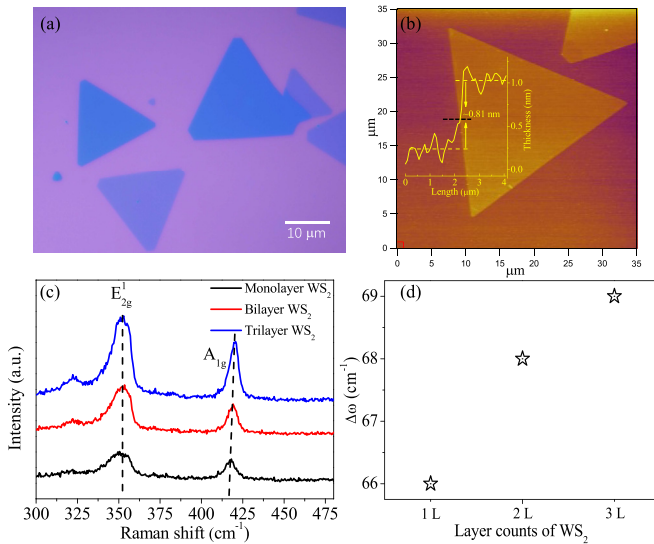


FIG. 1. (a) Optical image of WS₂ on SiO₂. (b) AFM image of the monolayer WS₂ and the corresponding height profile is inset. (c) Raman spectrum for the different WS₂ layer counts. (d) The frequency difference between E_{2g}¹ and A_{1g} modes as a function of the WS₂ layer counts.

transfer between WS₂ (1 and 3 L)/Co is much larger than that between WS₂ (2 L)/Co, which shares the same mechanism as the SOPE.

WS₂ were grown on a Si (p++)/SiO₂ (300 nm) substrate using the chemical vapor deposition method. Then the Co(3 nm)/Pt(3 nm) film was sputtered on the surface of WS₂. Finally, the Co/Pt film on the WS₂ flake was patterned in Hall bars for measuring anomalous Hall effect (AHE) [29,30]. The first-principles calculations based on self-consistent resolved the Kohn-Sham function and the projector augmented wave (PAW) pseudopotentials are implemented in Vienna *Ab initio* Simulation Package (VASP) [31,32]. The exchange-correlation potential is in the form of Perdew-Burke-Ernerhof (PBE) with the generalized gradient approximation (GGA). For structural optimization, the energy convergence threshold is set to 10⁻⁵ eV and the residual force on each atom is less than 0.05 eV/Å. The cutoff energy for the plane-wave basis is set to 450 eV. The Brillouin zone is sampled with Γ centered Monkhorst-Pack grids of 1 × 1 × 1. The PBE that formed with the van der Waals (vdW) correction (vdW-DF2) [33] is selected.

Figure 1(a) shows the typical triangle WS₂ flakes. The different color contrasts indicate that the grown WS₂ flakes have different layer counts, which were further checked by both the atomic force microscope (AFM) and the Raman spectroscopy. In Fig. 1(b), the height of WS₂ flake measured by AFM is ~0.81 nm, indicating a monolayer WS₂ flake [34]. As a typical WS₂ Raman spectroscopy, an in-plane vibrational E_{2g}¹ mode and an out-of-plane vibrational A_{1g} mode are both shown in Fig. 1(c). The E_{2g}¹ mode shows little dependence on the layers, while the blue shift appears in the A_{1g} mode with increasing layer counts of WS₂, due to the lattice stiffening effect when adding additional layers. Thus, the frequency differences ($\Delta\omega$) between the modes of E_{2g}¹ and A_{1g} can be

used to determine the layer counts of WS₂ flake. As shown in Fig. 1(d), the layer counts of WS₂ (1–3 L) are identified as $\Delta\omega \approx 66, 68,$ and 69 cm^{-1} , in consistent with the previous results [34].

Figure 2(a) shows the Hall bar of the WS₂/Co/Pt trilayer. The Hall resistances (R_{xy}) for different WS₂ layer counts in Fig. 2(b) are all saturated under an out-of-plane magnetic field at around $\pm 10 \text{ kOe}$ due to AHE. The almost zero coercivity indicates that the Co layer is in-plane anisotropy. However, one can easily find that the saturated Hall resistance (R_{xy}^{AHE}) depends on the WS₂ layer counts. When inserting the WS₂ layer, R_{xy}^{AHE} sharply drops, and the variation of the odd layer counts of WS₂ (1 and 3 L) is much larger than the even layer counts (2 L), as shown in Fig. 2(c). Interestingly, Fig. 2(d) further shows that the out-of-plane anisotropy field (H_K) exhibits similar behavior. Considering $R_{xy}^{\text{AHE}} \propto M_S$ [29], we ascribe this variation of R_{xy}^{AHE} to the origination of local magnetic moment in WS₂/Co due to the SOPE. Moreover, it is reasonable to consider that the Co magnetization is coherently rotated from in-plane to out-of-plane, and we can simply yield $H_K = 2K_u/M_S$. Thus, the variation of H_K also originates from the form of the local magnetic moment. In Fig. 2(e), the linear relationship between R_{xy}^{AHE} and H_K further supports our explanations, and excludes other reasons, i.e., the influence of interfacial roughness. Similar results have been reproduced in 12 independent devices.

The variation of coercivity with the addition of WS₂ is another important indicator of the SOPE. Figures 2(f)–2(i) show that the hysteresis loops of the WS₂/Co/Pt trilayer also depend on the WS₂ layer counts, when an in-plane magnetic field is applied along both the longitudinal and transversal directions of the Hall bar. The almost identical loops suggest that the sample is in-plane isotropic. In comparison to the Co/Pt bilayer coercivity [$\sim 44 \text{ Oe}$ in Fig. 2(f)], the coercivity of WS₂/Co/Pt trilayers decreased to $\sim 30 \text{ Oe}$ for WS₂ (1 and 3 L), while the coercivity of WS₂ (2 L) remained at $\sim 40 \text{ Oe}$ in Fig. 2(h). This behavior is similar to the variations of R_{xy}^{AHE} and H_K with increasing WS₂ layer counts in Fig. 2(e), suggesting the SOPE plays an important role for device magnetic properties.

Figures 3(a) and 3(b) show $R_{xy}^{1\omega}$ and $R_{xy}^{2\omega}$ curves of WS₂ (1 L)/Co/Pt trilayer, respectively. The $R_{xy}^{1\omega}$ curves exhibit apparent $R_{xy}^{\text{PHE}} \sin 2\varphi$ characters, as expected the planar Hall effect is dominated and the planar Hall resistance R_{xy}^{PHE} is fitted as 0.32Ω . The $R_{xy}^{2\omega}$ curves are given as [30]:

$$R_{xy}^{2\omega} = \left[\left(H_{\text{DL}} \frac{R_{xy}^{\text{AHE}}}{2(H_K - H)} + R_{\nabla T}^{2\omega} \right) \cos \varphi - (H_{\text{FL}} + H_{\text{Oe}}) \frac{R_{xy}^{\text{PHE}}}{H} \cos \varphi \cos 2\varphi \right], \quad (1)$$

where the R_{xy}^{AHE} and R_{xy}^{PHE} are the anomalous and planar Hall resistance, respectively, H_K is the out-of-plane anisotropy field, $R_{\nabla T}^{2\omega}$ is the thermal effect contribution, H_{DL} (H_{FL}) is the Dampinglike (fieldlike) effective field originating from SOT, and H_{Oe} is the Oersted field. Figures 3(c) and 3(d) summarize the dependences of $\cos \varphi$ and $\cos \varphi \cos 2\varphi$ component with the $1/(H_K - H)$ and $1/H$ under various current densities,

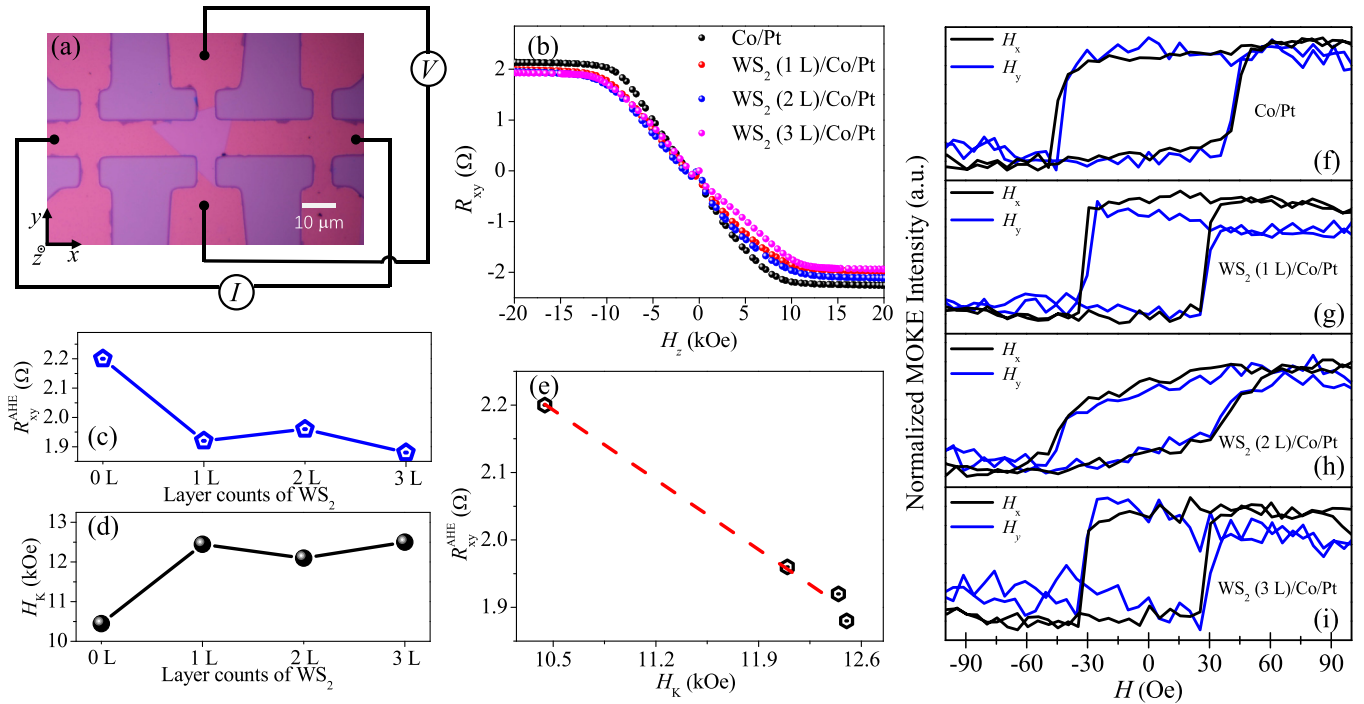


FIG. 2. (a) The optical image of the device and schematic of harmonic Hall measurement. (b) The Hall resistance of the WS₂ (0–3 L)/Co/Pt devices by sweeping the out-of-plane field. The extracted (c) R_{xy}^{AHE} and (d) H_K with the different WS₂ layer counts. (e) The dependence of the R_{xy}^{AHE} and H_K with the WS₂ layer counts (0–3 L). (f)–(i) Hysteresis loops of the WS₂ (0–3 L)/Co/Pt.

respectively, where the H_{DL} and the $(H_{FL} + H_{Oe})$ are obtained from the curve slopes. Noted that $R_{VT}^{2\omega}$ that also contributes a $\cos\varphi$ signal is independent of the external magnetic field, which can be excluded by the linear fitting analysis.

We obtain the current density dependence of H_{DL} and H_{FL} of different WS₂ layer counts, which are shown in Figs. 3(e) and 3(f), respectively. We define $h_{DL} = dH_{DL}/dJ$ to determine the SOT efficiency. First, as we expected, h_{DL} of different WS₂ layer counts are correlated to the parity of layer counts, as shown in Fig. 3(g). For the Co/Pt bilayer, h_{DL} for current density (J) 1×10^7 A/cm² is 27.33 Oe. However, for inserting the 1 and 3 L WS₂ layers, h_{DL} are sharply increased to 35.07 and 36.86 Oe, respectively, while $h_{DL} = 28.05$ Oe for WS₂ (2 L) is almost the same as the WS₂ (0 L). The error bars of SOT data are obtained by measuring 4, 5, and 3 samples for WS₂ (1, 2, and 3 L)/Co/Pt, respectively. Second, after subtracting the $H_{Oe} = J_{Pt}t_{Pt}/2$ induced by the current in the Pt layer [35], we find that the $h_{FL} = dH_{FL}/dJ$ is one order of amplitude smaller than h_{DL} . As shown in Fig. 3(h), when inserting the WS₂ layer, the h_{FL} could increase from 2.14 to 2.52, 3.15, and 2.91 Oe (per 1×10^7 A/cm²) for 1, 2, and 3 L, respectively. The small value of efficiency of H_{FL} may be attributed to the difference in local charge imbalances [36,37], which is somehow compensated by the hybridization and reduces the electric field at the interface. Finally, as shown in Figs. 3(i) and 3(j), the coercivity and R_{xy}^{AHE} have a linear correlation with WS₂ layer counts as h_{DL} dependencies, respectively. We notice that such layer-dependent behavior of WS₂ is also reported by Husain *et al.* [38]. For the WS₂/Co₃FeB bilayer, the temperature dependence of the Gilbert damping factor is controlled by WS₂ layer counts,

where the damping parameter reduces with decreasing temperature for the odd WS₂ layers (1 and 3 L), which is opposite to the WS₂ even layers (2 and 4 L).

We demonstrate current driven magnetization switching by using the magneto-optical Kerr effect (MOKE) microscopy. Owing to the y -polarized spin current is collinear to the easy axis of the FM, the in-plane magnetization can be switched directly by the SOT without an auxiliary magnetic field, which is similar to STT-induced magnetization switching [19,39]. Figures 4(a)–4(d) show a typical current induced magnetization switching in our WS₂ (1 L)/Co/Pt devices. We first set the magnetization along the Hall bar transverse direction ($+y$), and cut off the image background shown in Fig. 4(a). The current then gradually increases through the Hall bar. When a J of -3.00×10^7 A/cm² is used, the magnetization switching starts in the WS₂ region ($-y$), which is depicted as the white area in Fig. 4(b). This was attributed to both SOT enhancement and reduced coercivity caused by SOPE. When we further increase the current, as shown in Fig. 4(c)–4(d), the formed reverse domain wall gradually propagates to the whole Hall bar region. For our case that J is 3.00×10^7 A/cm² and t is 3 nm, Oersted field is only 5.65 Oe. Given that H_{Oe} is one magnitude less than the coercivity (29.90 Oe) of the Co/Pt layer and two magnitudes less than SOT field ($H_{DL} = 105.21$ Oe), we think that Oersted field is negligible in the magnetization switching process. No reverse domain wall in other region strongly suggests that inserting WS₂ indeed decreases the critical current density for the whole device.

Finally, both the coercivity and the SOT efficiency dependence of the WS₂ layer counts can be understood by the SOPE. The WS₂ is regarded as a semiconductor with strong

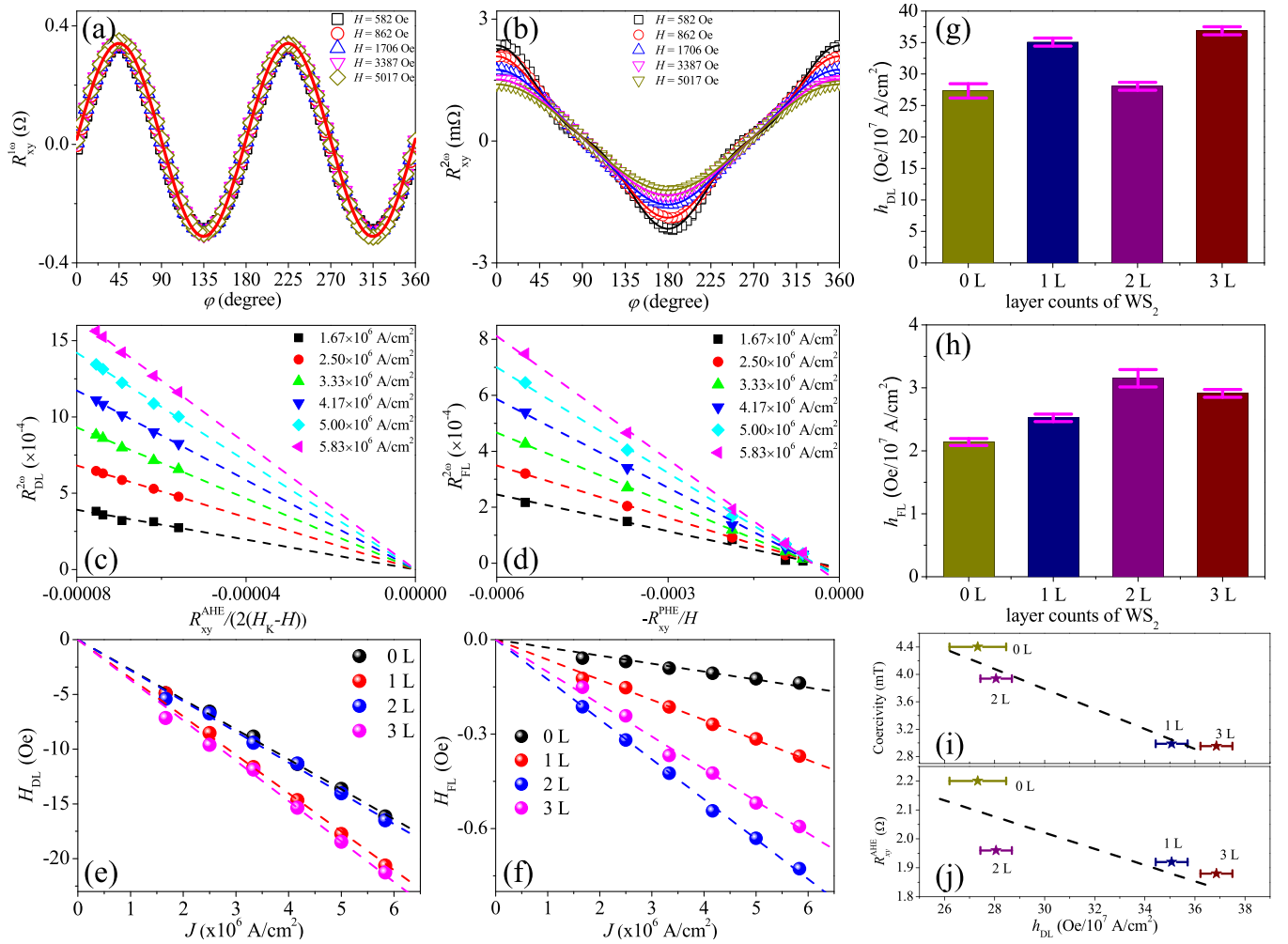


FIG. 3. (a) First and (b) second harmonic Hall resistance as a function of the azimuthal ϕ under various external field for the WS₂ (1 L)/Co/Pt device at $J = 5.00 \times 10^6$ A/cm². The linear fitting to (c) $R_{\text{DL}}^{2\omega}$ vs. $R_{\text{xy}}^{\text{AHE}}/[2(H_{\text{k}}-H)]$ and (d) $R_{\text{FL}}^{2\omega}$ vs. $R_{\text{xy}}^{\text{PHE}}/H$ for the WS₂ (1 L)/Co/Pt. The SOT effective fields of (e) H_{DL} and (f) H_{FL} as a function of the current density J for the WS₂ (0–3 L)/Co/Pt trilayer. The SOT efficiency of (g) h_{DL} and (h) h_{FL} as a function of the WS₂ layer counts. The relationship between h_{DL} and the (i) coercivity and (j) $R_{\text{xy}}^{\text{AHE}}$ with the WS₂ (0–3 L).

SOC, which could lead to the hybridization of the wave function between WS₂ and Co. The charge transfer appears from WS₂ to Co during the hybridization of wave function. The decrease of the Co atom spin magnetic moment is expected, which is manifested as the reduction of coercivity and $R_{\text{xy}}^{\text{AHE}}$.

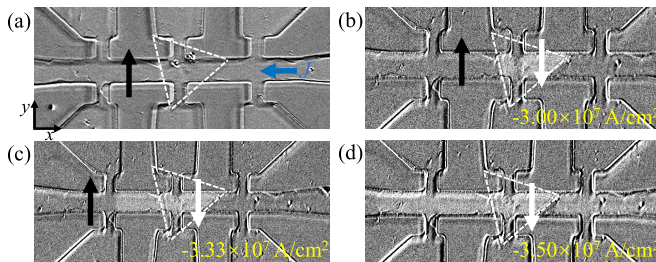


FIG. 4. (a)–(d) Evolution of magnetic domains by MOKE with applying different current pulses. The blue arrow means the current direction along $-x$. The black and white arrows mean the magnetization directions along $+y$ and $-y$, respectively.

This is similar to the theory reported by Garandel *et al.* in MoS₂/Co bilayer [40], where the charge can be transferred due to covalent bonding between S and Co atoms, and the bonding becomes metallic due to hybridization between S p and Co d orbitals. This bonding also allows spin to be injected into the MoS₂, not only causing the decrease of the Co atom spin magnetic moment, but also inducing the nonequilibrium spin density, whose cross product with the magnetization of Co determines an additional SOT. Unfortunately, the x - and/or z -polarized spin current is not detected in our experiment. This could be due to the fact that H-WS₂ has C_{3v} symmetry rather than C_{1v} symmetry like T_d-WTe₂, where the unconventional torque cannot be observed based on symmetry analysis [41]. Moreover, the additional torque might also be coming from the spin accumulation and SHE in Pt, which needs further study later.

To explore the charge transfer at the WS₂/Co interface, the charge density difference of the WS₂ (1–3 L)/Co heterostructures were calculated, and the results are depicted

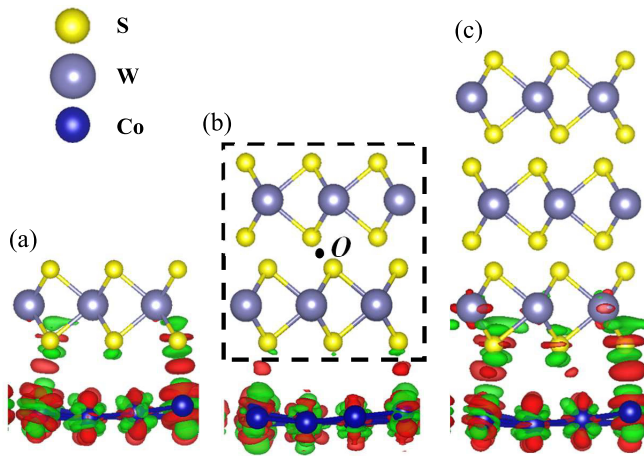


FIG. 5. The side view of the charge density differences for (a) WS₂ (1 L)/Co, (b) WS₂ (2 L)/Co, and (c) WS₂ (3 L)/Co, respectively. The black dotted area in (b) is the schematic for the inversion symmetry and the center (*O*) for WS₂ (2 L).

in Figs. 5(a)–5(c). To eliminate interaction between periodically adjacent WS₂ layers, we use the thickness of the vacuum exceeding 15 Å along the *z* direction. To construct the WS₂/Co heterostructure, we take 3 × 3WS₂ (1–3 L) to match 4 × 4 single layer Co with a minimum mismatch of lattice constants. The charge density difference ($\Delta\rho$) is obtained by subtracting the charges of WS₂ and Co from those of the heterostructure WS₂/Co as $\Delta\rho = \rho_{(\text{WS}_2/\text{Co})} - \rho_{(\text{WS}_2)} - \rho_{(\text{Co})}$, where $\rho_{(\text{WS}_2/\text{Co})}$, $\rho_{(\text{WS}_2)}$ and $\rho_{(\text{Co})}$ are the charge densities of the heterostructure WS₂/Co, WS₂, and Co, respectively. Figures 5(a)–5(c) show side views of the calculated charge transfer at the WS₂ (1–3 L)/Co interface. The red region represents charge dissipation, and the green region indicates charge accumulation. As expected, we see that charge transfer occurs between the interface of S and Co atoms along S-Co covalent bonds. The charge redistribution mainly occurs at the WS₂ (1 L)/Co and WS₂ (3 L)/Co interface regions. We can see that there are areas of electron accumulation/dissipation around each atom at the interface. On the whole, the electrons on the interface are transferred from the WS₂ layer to the Co

layer. Such an obvious unbalance of electron accumulation and dissipation at the interface induces a built-in electric field pointing from WS₂ to Co. Due to the charge transfer, the net residual magnetic moment increases on WS₂, enhancing the SOT of the devices, whereas almost no charge transfer is observed in the interface region of WS₂ (2 L)/Co, which could be in great agreement with our experimental results.

Moreover, the WS₂ layer counts dependence of enhanced SOT could also be understood through the protection of inversion symmetry [38,42,43]. As shown in the black dotted area in Fig. 5(b), there is an inverse symmetric center point *O* in WS₂ (2 L), but absence in WS₂ (1 and 3 L). The hybridization of the wave function would be prohibited due to the protection of inversion symmetry of WS₂ (2 L). Theoretically, the inversion symmetry breaking together with spin-orbit coupling has been discussed by Yao and Xiao *et al.* [42,43], which leads to coupled spin and valley physics in monolayers of MoS₂ and other TMDs. Our results are consistent with theoretical predictions in the high-quality and different layer counts of WS₂. Unlike other similar SOT-based 2D materials work, such as the spin source [14–17,19,44] and spin sink [21,22,45], the correlation between the FM and TMDs plays more important role in generation spin current, in particular the spin polarization direction depends on the magnetization of FM. This feature could be a breakthrough for the exploration of spin-dependent transport phenomena in TMDs-based devices.

In conclusion, we demonstrated the variation of coercivity and SOT of WS₂/Co/Pt trilayers modulated by inserting the WS₂ layer counts. The variation of coercivity and SOT efficiency have the identical dependence on WS₂ layer counts due to SOPE. We expect our result to provide an efficient route for material engineering towards improved SOT-based spintronic devices.

This work is supported by the National Natural Science Foundation of China (Grants No. 11774139, No. 11874189, and No. 91963201), Program for Changjiang Scholars and Innovative Research Team in University (Grant No. IRT-16R35)), the 111 Project under Grant No. B20063, and Fundamental Research Funds for the Central Universities lzujbky-2021-ct01.

- [1] X. Qiu, W. Legrand, P. He, Y. Wu, J. Yu, R. Ramaswamy, A. Manchon, and H. Yang, Enhanced Spin-Orbit Torque via Modulation of Spin Current Absorption, *Phys. Rev. Lett.* **117**, 217206 (2016).
- [2] Y. Hibino, T. Hirai, K. Hasegawa, T. Koyama, and D. Chiba, Enhancement of the spin-orbit torque in a Pt/Co system with a naturally oxidized Co layer, *Appl. Phys. Lett.* **111**, 132404 (2017).
- [3] L. Zhou, V. L. Grigoryan, S. Maekawa, X. Wang, and J. Xiao, Spin Hall effect by surface roughness, *Phys. Rev. B* **91**, 045407 (2015).
- [4] S. Woo, M. Mann, A. J. Tan, L. Caretta, and G. S. D. Beach, Enhanced spin-orbit torques in Pt/Co/Ta heterostructures, *Appl. Phys. Lett.* **105**, 212404 (2014).
- [5] J. Yu, X. Qiu, W. Legrand, and H. Yang, Large spin-orbit torques in Pt/Co-Ni/W heterostructures, *Appl. Phys. Lett.* **109**, 042403 (2016).
- [6] H.-Y. Lee, S. Kim, J.-Y. Park, Y.-W. Oh, S.-Y. Park, W. Ham, Y. Kotani, T. Nakamura, M. Suzuki, T. Ono, K.-J. Lee, and B.-G. Park, Enhanced spin-orbit torque via interface engineering in Pt/CoFeB/MgO heterostructures, *APL Mater.* **7**, 031110 (2019).
- [7] X. Qiu, K. Narayanapillai, Y. Wu, P. Deorani, D.-H. Yang, W.-S. Noh, J.-H. Park, K.-J. Lee, H.-W. Lee, and H. Yang, Spin-orbit-torque engineering via oxygen manipulation, *Nature Nanotechnol.* **10**, 333 (2015).
- [8] H. Wang, J. Kally, J. S. Lee, T. Liu, H. Chang, D. R. Hickey, K. A. Mkhoyan, M. Wu, A. Richardella, and N. Samarth, Surface-State-Dominated Spin-Charge Current

- Conversion in Topological-Insulator-Ferromagnetic-Insulator Heterostructures, *Phys. Rev. Lett.* **117**, 076601 (2016).
- [9] Y. Fan, X. Kou, P. Upadhyaya, Q. Shao, L. Pan, M. Lang, X. Che, J. Tang, M. Montazeri, K. Murata, L.-T. Chang, M. Akyol, G. Yu, T. Nie, K. L. Wong, J. Liu, Y. Wang, Y. Tserkovnyak, and K. L. Wang, Electric-field control of spin-orbit torque in a magnetically doped topological insulator, *Nature Nanotechnol.* **11**, 352 (2016).
- [10] D. Go, D. Jo, C. Kim, and H.-W. Lee, Intrinsic Spin and Orbital Hall Effects from Orbital Texture, *Phys. Rev. Lett.* **121**, 086602 (2018).
- [11] D. Go and H.-W. Lee, Orbital torque: Torque generation by orbital current injection, *Phys. Rev. Res.* **2**, 013177 (2020).
- [12] A. Davidson, V. P. Amin, W. S. Aljuaid, P. M. Haney, and X. Fan, Perspectives of electrically generated spin currents in ferromagnetic materials, *Phys. Lett. A* **384**, 126228 (2020).
- [13] W. Wang, Z. Yan, Y. Cao, C. Gao, Z. Shi, M. Si, J. Cao, L. Xi, D. Yang, and D. Xue, Generation and detection of Dresselhaus-like spin current in a single-crystal ferromagnetic metal, *Adv. Funct. Mater.* **32**, 2204212 (2022).
- [14] Q. Shao, G. Yu, Y.-W. Lan, Y. Shi, M.-Y. Li, C. Zheng, X. Zhu, L.-J. Li, P. K. Amiri, and K. L. Wang, Strong Rashba-Edelstein effect-induced spin-orbit torques in monolayer transition metal dichalcogenide/ferromagnet bilayers, *Nano Lett.* **16**, 7514 (2016).
- [15] W. Lv, Z. Jia, B. Wang, Y. Lu, X. Luo, B. Zhang, Z. Zeng, and Z. Liu, Electric-field control of spin-orbit torques in WS₂/permalloy bilayers, *ACS Appl. Mater. Interfaces* **10**, 2843 (2018).
- [16] S. Novakov, B. Jariwala, N. M. Vu, A. Kozhakhmetov, J. A. Robinson, and J. T. Heron, Interface transparency and Rashba spin torque enhancement in WSe₂ heterostructures, *ACS Appl. Mater. Interfaces* **13**, 13744 (2021).
- [17] D. MacNeill, G. M. Stiehl, M. H. D. Guimaraes, R. A. Buhrman, J. Park, and D. C. Ralph, Control of spin-orbit torques through crystal symmetry in WTe₂/ferromagnet bilayers, *Nature Phys.* **13**, 300 (2017).
- [18] D. MacNeill, G. M. Stiehl, M. H. D. Guimaraes, N. D. Reynolds, R. A. Buhrman, and D. C. Ralph, Thickness dependence of spin-orbit torques generated by WTe₂, *Phys. Rev. B* **96**, 054450 (2017).
- [19] S. Shi, J. Li, C. Hsu, K. Lee, Y. Wang, L. Yang, J. Wang, Q. Wang, H. Wu, W. Zhang, G. Eda, G. Liang, H. Chang, and H. Yang, Observation of the out-of-plane polarized spin current from CVD grown WTe₂, *Adv. Quantum Tech.* **4**, 2100038 (2021).
- [20] X. Chen, S. Shi, G. Shi, X. Fan, C. Song, X. Zhou, H. Bai, L. Liao, Y. Zhou, H. Zhang, A. Li, Y. Chen, X. Han, S. Jiang, Z. Zhu, H. Wu, X. Wang, D. Xue, H. Yang, and F. Pan, Observation of the antiferromagnetic spin Hall effect, *Nature Mater.* **20**, 800 (2021).
- [21] P. Debashis, T. Y. T. Hung, and Z. Chen, Monolayer WSe₂ induced giant enhancement in the spin Hall efficiency of Tantalum, *npj 2D Mater. Appl.* **4**, 18 (2020).
- [22] H. Xue, M. Tang, Y. Zhang, Z. Ji, X. Qiu, and Z. Zhang, Giant enhancement of spin-orbit torque efficiency in Pt/Co bilayers by inserting a WSe₂ under layer, *Adv. Electron. Mater.* **8**, 2100684 (2022).
- [23] K. Dolui and B. K. Nikolic, Spin-orbit-proximitized ferromagnetic metal by monolayer transition metal dichalcogenide: Atlas of spectral functions, spin textures, and spin-orbit torques in Co/MoSe₂, Co/WSe₂, and Co/TaSe₂ heterostructures, *Phys. Rev. Mater.* **4**, 104007 (2020).
- [24] S. Y. Huang, X. Fan, D. Qu, Y. P. Chen, W. G. Wang, J. Wu, T. Y. Chen, J. Q. Xiao, and C. L. Chien, Transport Magnetic Proximity Effects in Platinum, *Phys. Rev. Lett.* **109**, 107204 (2012).
- [25] B. Scharf, G. Xu, A. Matos-Abiague, and I. Zutic, Magnetic Proximity Effects in Transition-Metal Dichalcogenides: Converting Excitons, *Phys. Rev. Lett.* **119**, 127403 (2017).
- [26] K. Dolui, M. D. Petrović, K. Zollner, P. Plecháč, J. Fabian, and B. K. Nikolić, Proximity spin-orbit torque on a two-dimensional magnet within van der Waals heterostructure: Current-driven antiferromagnet-to-ferromagnet reversible nonequilibrium phase transition in bilayer CrI₃, *Nano Lett.* **20**, 2288 (2020).
- [27] S. Fukami, T. Anekawa, C. Zhang, and H. Ohno, A spin-orbit torque switching scheme with collinear magnetic easy axis and current configuration, *Nature Nanotechnol.* **11**, 621 (2016).
- [28] X. Han, X. Wang, C. Wan, G. Yu, and X. Lv, Spin-orbit torques: Materials, physics, and devices, *Appl. Phys. Lett.* **118**, 120502 (2021).
- [29] S. Sangiao, L. Morellon, G. Simon, J. M. De Teresa, J. A. Pardo, J. Arbiol, and M. R. Ibarra, Anomalous Hall effect in Fe(001) epitaxial thin films over a wide range in conductivity, *Phys. Rev. B* **79**, 014431 (2009).
- [30] C. O. Avci, K. Garello, M. Gabureac, A. Ghosh, A. Fuhrer, S. F. Alvarado, and P. Gambardella, Interplay of spin-orbit torque and thermoelectric effects in ferromagnet/normal-metal bilayers, *Phys. Rev. B* **90**, 224427 (2014).
- [31] G. Kresse and J. Furthmüller, Efficiency of *ab initio* total energy calculations for metals and semiconductors using a plane-wave basis set, *Comput. Mater. Sci.* **6**, 15 (1996).
- [32] G. Kresse and J. Furthmüller, Efficient iterative schemes for *ab initio* total-energy calculations using a plane-wave basis set, *Phys. Rev. B* **54**, 11169 (1996).
- [33] S. Grimme, Semiempirical GGA-type density functional constructed with a long-range dispersion correction, *J. Comput. Chem.* **27**, 1787 (2006).
- [34] H. Zeng, G.-B. Liu, J. Dai, Y. Yan, B. Zhu, R. He, L. Xie, S. Xu, X. Chen, W. Yao, and X. Cui, Optical signature of symmetry variations and spin-valley coupling in atomically thin tungsten dichalcogenides, *Sci. Rep.* **3**, 1608 (2013).
- [35] B. Han, B. Wang, Z. Yan, T. Wang, D. Yang, X. Fan, Y. Wang, and J. Cao, Determination of the Spin-Orbit Torques in Ferromagnetic-Heavy-Metal Bilayers Using Harmonic Longitudinal Voltage Measurements, *Phys. Rev. Appl.* **13**, 014065 (2020).
- [36] J. J. Palacios, J. Fernandez-Rossier, and L. Brey, Vacancy-induced magnetism in graphene and graphene ribbons, *Phys. Rev. B* **77**, 195428 (2008).
- [37] A. Tagliacozzo, G. Campagnano, D. Giuliano, P. Lucignano, and B. Jouault, Thermal transport driven by charge imbalance in graphene in a magnetic field close to the charge neutrality point at low temperature: Nonlocal resistance, *Phys. Rev. B* **99**, 155417 (2019).
- [38] S. Husain, S. Pal, X. Chen, P. Kumar, A. Kumar, A. K. Mondal, N. Behera, N. K. Gupta, S. Hait, R. Gupta, R. Brucas, B. Sanyal, A. Barman, S. Chaudhary, and P. Svedlindh, Large Dzyaloshinskii-Moriya interaction and atomic layer thickness

- dependence in a ferromagnet-WS₂ heterostructure, *Phys. Rev. B* **105**, 064422 (2022).
- [39] Y. Wang, D. Zhu, Y. Yang, K. Lee, R. Mishra, G. Go, S.-H. Oh, D.-H. Kim, K. Cai, E. Liu, S. D. Pollard, S. Shi, J. Lee, K. L. Teo, Y. Wu, K.-J. Lee, and H. Yang, Magnetization switching by magnon-mediated spin torque through an antiferromagnetic insulator, *Science* **366**, 1125 (2019).
- [40] T. Garandel, R. Arras, X. Marie, P. Renucci, and L. Calmels, Electronic structure of the Co(0001)/MoS₂ interface and its possible use for electrical spin injection in a single MoS₂ layer, *Phys. Rev. B* **95**, 075402 (2017).
- [41] Y. Liu and Q. Shao, Two-dimensional materials for energy-efficient spin-orbit torque devices, *ACS Nano* **14**, 9389 (2020).
- [42] D. Xiao, G.-B. Liu, W. Feng, X. Xu, and W. Yao, Coupled Spin and Valley Physics in Monolayers of MoS₂ and Other Group-VI Dichalcogenides, *Phys. Rev. Lett.* **108**, 196802 (2012).
- [43] W. Yao, D. Xiao, and Q. Niu, Valley-dependent optoelectronics from inversion symmetry breaking, *Phys. Rev. B* **77**, 235406 (2008).
- [44] W. Lv, J. Cai, Z. Li, W. Lv, Y. Shao, S. Li, B. Zhang, Y. Chang, Z. Liu, and Z. Zeng, Current-induced torques in black phosphorus/permalloy bilayers due to crystal symmetry, *Appl. Phys. Lett.* **117**, 062403 (2020).
- [45] W. Lv, H. Xue, J. Cai, Q. Chen, B. Zhang, Z. Zhang, and Z. Zeng, Enhancement of spin-orbit torque in WTe₂/perpendicular magnetic anisotropy heterostructures, *Appl. Phys. Lett.* **118**, 052406 (2021).